Journal of Solid Mechanics Vol. 4, No. 4 (2012) pp. 339-354

Analytical Solution for Electro-mechanical Behavior of Piezoelectric Rotating Shaft Reinforced by BNNTs Under Non-axisymmetric Internal Pressure

A. Ghorbanpour Arani[1,2*], E. Haghparast[1], S. Amir[1]

[1]*Faculty of Mechanical Engineering, University of Kashan, Kashan, Islamic Republic of Iran*
[2]*Institute of Nanoscience & Nanotechnology, University of Kashan, Kashan, Islamic Republic of Iran*

Received 14 September 2012; accepted 11 November 2012

ABSTRACT

In this study, two-dimensional electro-mechanical analysis of a composite rotating shaft subjected to non-axisymmetric internal pressure and applied voltage is investigated where hollow piezoelectric shaft reinforced by boron nitride nanotubes (BNNTs). Composite structure is modeled based on piezoelectric fiber reinforced composite (PFRC) theory and a representative volume element has been considered for predicting the elastic, piezoelectric and dielectric properties of the composite rotating shaft. Distribution of radial, circumferential, shear and effective stresses and electric displacement in composite rotating shaft are determined based on Fourier series. The detailed parametric study is conducted, focusing on the remarkable effects of angular velocity, electric potential, volume fraction and orientation angle of BNNTs on the distribution of stresses. The results show that properties of the piezoelectric shaft as matrix have significant influence on the electro-mechanical stresses where the PZT-4 has less effective stresses against PVDF. Therefore, PZT-4 could be considered for improving optimum design of rotating piezoelectric shaft under electric field and non-axisymmetric mechanical loadings.

Keywords: Composite rotating shaft; Micro-electro-mechanical model; Non-axisymmetric pressure; BNNTs fiber

1 INTRODUCTION

COMPOSITES offer advantageous characteristics of different materials with qualities that none of the constituents possess. Smart composite shaft addressed in this paper has been attracted more attention amongst researchers due to provision of new properties and exploiting unique synergism between materials. Piezoelectric materials produce an electric field when deformed, and undergo deformation when subjected to an electric field. The coupling nature of piezoelectric materials has attracted wide applications in electro-mechanical and electrical devices, such as actuators, sensors and transducers. PZT_4 is an ideal piezoelectric matrix due to excellent mechanical properties. In this work, BNNTs are selected as the matrix reinforcements, apart from having high mechanical, electrical, thermal conductivity and chemical properties, present more resistant to oxidation than other conventional nano-reinforcements such as carbon nanotubes (CNTs).

* Corresponding author. Tel.: +98 9131626594 ; Fax: +98 361 55912424.
E-mail address: aghorban@kashanu.ac.ir (A.Ghorbanpour Arani).

In recent years, most of the research works are concentrated on the analytical electro-thermo- mechanical stress solutions of disks and shafts. Mechanical and thermal stresses in a FG rotating disk with variable thickness due to radially symmetry loads reported by Bayat et al. [1] who considered a rotating FG disk with variable thickness under a steady temperature field. They found that maximum values of radial stresses due to thermo-mechanical loading in FG hollow disks with variable thickness under free–free condition remain in between the maximum values for homogenized disks. Contrary to this, radial stresses for FG disks due to thermal load may not occur in between the radial stresses for full-ceramic and full-metal disks. Hojjati et al. [2] developed the Semi-exact solution of non-uniform thickness and density rotating disks. Their study demonstrated that more efficient and economical design can be achieved by permitting elastic–plastic deformation and by an appropriate choice of the thickness parameters in the applications. Babaei et al. [3] presented analytical solution for a radially piezoelectric functionally graded piezoelectric (FGP) rotating hollow shaft subjected to electrical and mechanical loads. They showed that for rotating shaft with specific radial stress boundary conditions, changes in the electric boundary conditions cannot decrease the hoop stress value below a fixed amount. Ghorbanpour Arani et al. [4] investigated the effect of material in-homogeneity on electro-thermo-mechanical behaviors of functionally graded piezoelectric rotating shaft. They found that the material in-homogeneity has a significant influence on the electro-thermo- mechanical stresses, radial displacement and electric potential and hence should be considered in optimum design. Also, Ghorbanpour Arani et al. [5] investigated the nonlinear vibration and stability analysis of a polymeric composite smart micro-tube reinforced by BNNTs. They found that stability of the micro-tube is strongly dependent on imposed electric potential, where increasing the imposed positive electric potential significantly increases the stability of the system. Also, their results showed using BNNTs as a piezoelectric fiber and its orientation angle with respect to micro-tube axis have significant effects on the vibration response and stability of the system. The stress response and onset of yield of rotating FGM hollow shafts is studied by Akis et al. [6]. Their study revealed that a rotating FGM hollow shaft may yield at one or both of the free surfaces or somewhere inside the shaft. Nevertheless, considerable improvement in the performance of an FGM hollow shaft is possible if the modulus of elasticity is an increasing, and the yield strength is a decreasing function of the radial coordinate. Electro-magneto-mechanical responses of a radially polarized rotating functionally graded piezoelectric shaft are presented by Ghorbanpour Arani et al. [7] who focused on the β exponent in functionally graded materials. Their result showed that the β exponent significantly affected the radial and circumferential stress distributions, electric potential and magnetic field. This implies that the electro-magneto-mechanical fields in the rotating shaft should be optimized for any specific application by selecting the appropriate β exponent. The analytical solution of FG piezoelectric hollow cylinder which is under radial electric potential and non-axisymmetric thermo-mechanical loads are presented by Atrian et al. [8] who used complex Fourier series to indicate distributions of stresses, displacement and the effect of electric potential field on the cylinder behavior.

However, to date, no report has been found in the literature on the stress analysis of piezoelectric rotating shaft reinforced by BNNTs under non-axisymmetric internal pressure. Motivated by these considerations, the need for the investigation of a BNNTs fiber is applied as reinforcement in rotating shaft where PZT-4 has been selected for matrix as piezoelectric material. Composite rotating shaft subjected to uniform electric potential and non-axisymmetric internal pressure. Higher order governing equations are derived analytically and effects of non-axisymmetric internal pressure, electric potential, volume fraction and orientation angle of BNNTs on the stresses are investigated. Results of this research could be used for optimum design of composite rotating shaft under electric field and non-axisymmetric mechanical loadings.

2 STRESS ANALYSES

Composite rotating shaft reinforced by BNNTs subjected to non-axisymmetric internal pressure and applied voltage has been demonstrated in Fig. 1. The strain-displacement relations in cylindrical coordinate can be written as [9]:

$$\varepsilon_{rr} = \frac{\partial u}{\partial r} \ , \qquad \varepsilon_{\theta\theta} = \frac{1}{r}(\frac{\partial v}{\partial \theta}) + \frac{u}{r} \ , \qquad \varepsilon_{r\theta} = \frac{1}{2}\left(\frac{1}{r}(\frac{\partial u}{\partial \theta}) + \frac{\partial v}{\partial r} - \frac{v}{r}\right). \tag{1}$$

where u and v are components of displacement in radial and circumferential, respectively.

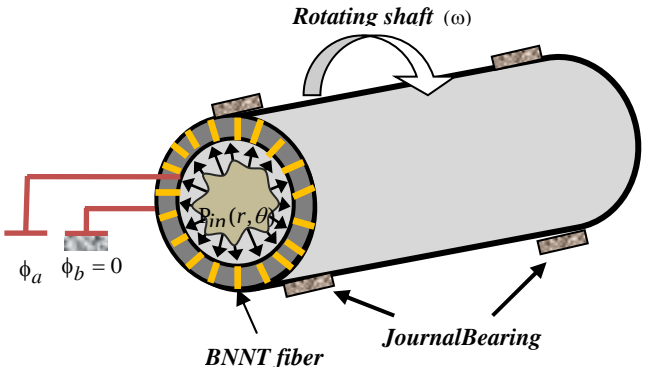

Fig. 1
The schematic of composite rotating shaft subjected to non-axisymmetric internal pressure and applied voltage ϕ_a.

2.1 Micro-electro-mechanical model

To model smart composite structures, a micromechanical model known as ''XY PEFRC'' or ''YX PEFRC'', using approach adopted by Tan and Tong [10], is employed. Based on this modeling, the reinforced BNNTs are considered as longitudinal straight fibers placed in PZT-4 matrix. In general case, to evaluate the effective properties of a PFRC unit cell in all directions, first the properties of the required strip is obtained in which an appropriate 'X model' in association with the 'Y model' (or vice versa), i.e., 'XY (or YX) rectangle model' has been employed. In this modeling, both matrix and reinforcements are assumed to be smart and polarization have been made along the fiber direction. According to the XY PEFRC micromechanical method, the constitutive equations for the electro-thermo-mechanical behavior of the selected RVE are expressed as [12]:

$$\begin{Bmatrix} \sigma \\ D \end{Bmatrix} = \begin{bmatrix} C & -e \\ e^T & \in \end{bmatrix} \begin{Bmatrix} \varepsilon \\ E \end{Bmatrix}. \tag{2}$$

where σ, ε, D and E are stress, strain, electric displacement and electric field vectors, respectively and $[e]$ and $[\in]$ are matrices of piezoelectric and dielectric parameters respectively. Eq. (2) can be expanded as follows:

$$\begin{Bmatrix} \sigma_1 \\ \sigma_2 \\ \sigma_3 \\ \tau_{23} \\ \tau_{31} \\ \tau_{12} \\ D_1 \\ D_2 \\ D_3 \end{Bmatrix} = \begin{bmatrix} C_{11} & C_{12} & C_{13} & 0 & 0 & 0 & 0 & 0 & -e_{31} \\ C_{12} & C_{22} & C_{23} & 0 & 0 & 0 & 0 & 0 & -e_{32} \\ C_{13} & C_{23} & C_{33} & 0 & 0 & 0 & 0 & 0 & -e_{33} \\ 0 & 0 & 0 & C_{44} & 0 & 0 & 0 & -e_{24} & 0 \\ 0 & 0 & 0 & 0 & C_{55} & 0 & -e_{15} & 0 & 0 \\ 0 & 0 & 0 & 0 & 0 & C_{66} & 0 & 0 & 0 \\ 0 & 0 & 0 & 0 & e_{15} & 0 & \in_{11} & 0 & 0 \\ 0 & 0 & 0 & e_{24} & 0 & 0 & 0 & \in_{22} & 0 \\ e_{31} & e_{32} & e_{33} & 0 & 0 & 0 & 0 & 0 & \in_{33} \end{bmatrix} \begin{Bmatrix} \varepsilon_1 \\ \varepsilon_2 \\ \varepsilon_3 \\ \gamma_{23} \\ \gamma_{31} \\ \gamma_{12} \\ E_1 \\ E_2 \\ E_3 \end{Bmatrix}. \tag{3}$$

Assuming plane strain condition and unidirectional electric field along the radius of rotating shaft Eq. (3) reduced to [5]:

$$\begin{Bmatrix} \sigma_{rr} \\ \sigma_{\theta\theta} \\ \tau_{r\theta} \\ D_r \end{Bmatrix} = [Q] \begin{Bmatrix} \varepsilon_{rr} \\ \varepsilon_{\theta\theta} \\ \gamma_{r\theta} \\ E_r \end{Bmatrix}. \tag{4}$$

where matrix $[Q]$ is defined as [5]:

$$[Q]=\begin{bmatrix} C_{rrrr} & C_{rr\theta\theta} & 0 & -e_{rrr} \\ C_{rr\theta\theta} & C_{\theta\theta\theta\theta} & 0 & -e_{r\theta\theta} \\ 0 & 0 & C_{r\theta r\theta} & 0 \\ e_{rrr} & e_{r\theta\theta} & 0 & \in_r \end{bmatrix}. \tag{5}$$

Electric field in radial direction of cylindrical coordinate for piezoelectric materials is [9]:

$$E_r=-\frac{\partial\phi}{\partial r}. \tag{6}$$

where ϕ denotes the scalar function of electric potential. To consider the effects of orientation angle of the BNNTs with respect to longitudinal axis, the following transformation matrix can be employed as [5]:

$$\left[\tilde{Q}\right]=[T][Q][T]^T. \tag{7}$$

The transformation matrix $[T]$ is:

$$[T]=\begin{bmatrix} \cos^2\alpha & \sin^2\alpha & 2\sin\alpha\cos\alpha & 0 \\ \sin^2\alpha & \cos^2\alpha & 2\sin\alpha\cos\alpha & 0 \\ -\sin\alpha\cos\alpha & \sin\alpha\cos\alpha & \cos^2\alpha-\sin^2\alpha & 0 \\ 0 & 0 & 0 & 1 \end{bmatrix}. \tag{8}$$

where α is the angle of BNNTs with respect to longitudinal axis of rotating shaft.

2.2 Equilibrium equations

The equilibrium equations of the composite rotating shaft in the radial and circumferential directions, irrespective of the body force and the charge equation of electrostatic are expressed as [7,9]:

$$\frac{\partial\sigma_{rr}}{\partial r}+\frac{1}{r}\frac{\partial\sigma_{r\theta}}{\partial\theta}+\frac{\sigma_{rr}-\sigma_{\theta\theta}}{r}+\rho r\omega^2=0, \tag{9a}$$

$$\frac{\partial\sigma_{r\theta}}{\partial r}+\frac{1}{r}\frac{\partial\sigma_{\theta\theta}}{\partial\theta}+\frac{2\,\sigma_{r\theta}}{r}=0, \tag{9b}$$

$$\frac{\partial D_r}{\partial r}+\frac{D_r}{r}=0. \tag{9c}$$

Using Eqs. (9), (1) and (4), the final equilibrium equations in terms of displacements and electrical potential can be determined as follows:

$$d_1\frac{\partial^2 u}{\partial r^2}+\frac{d_2}{r}\frac{\partial u}{\partial r}+\frac{d_3}{r^2}u+\frac{d_4}{r^2}\frac{\partial^2 u}{\partial\theta^2}+\frac{d_5}{r}\frac{\partial^2 v}{\partial r\,\partial\theta}+\frac{d_6}{r^2}\frac{\partial v}{\partial\theta}+d_7\frac{\partial^2\phi}{\partial r^2}+\frac{d_8}{r}\frac{\partial\phi}{\partial r}=-\rho r\omega^2, \tag{10a}$$

$$d_9\frac{\partial^2 v}{\partial r^2}+\frac{d_{10}}{r}\frac{\partial v}{\partial r}+\frac{d_{11}}{r^2}v+\frac{d_{12}}{r^2}\frac{\partial^2 v}{\partial\theta^2}+\frac{d_{13}}{r}\frac{\partial^2 u}{\partial r\,\partial\theta}+\frac{d_{14}}{r^2}\frac{\partial u}{\partial\theta}+\frac{d_{15}}{r^2}\frac{\partial^2\phi}{\partial r\,\partial\theta}=0, \tag{10b}$$

$$d_{16}\frac{\partial^2\phi}{\partial r^2}+\frac{d_{17}}{r}\frac{\partial\phi}{\partial r}+d_{18}\frac{\partial^2 u}{\partial r^2}+\frac{d_{19}}{r}\frac{\partial u}{\partial r}+\frac{d_{20}}{r}\frac{\partial^2 v}{\partial r\,\partial\theta}=0. \tag{10c}$$

where the constants d_1 to d_{20} are given in the Appendix A.

3 SOLVING PROCEDURE

3.1 General solution

Eqs. (10a) to (10c) are governing equations for a composite rotating shaft under electro-mechanical fields. In general solution of Eqs. (10), the radial, circumferential displacements and electric potential are presumed according to complex Fourier series form [9]:

$$\begin{aligned} u^g(r,\theta)&=\sum_{n=-\infty}^{\infty}u_n(r)e^{in\theta},\\ v^g(r,\theta)&=\sum_{n=-\infty}^{\infty}v_n(r)e^{in\theta},\\ \phi^g(r,\theta)&=\sum_{n=-\infty}^{\infty}\phi_n(r)e^{in\theta}=\phi_0(r). \end{aligned} \tag{11}$$

where $u_n(r)$ and $v_n(r)$ are the coefficients of complex Fourier series of $u(r,\theta)$ and $v(r,\theta)$, respectively, that can be expressed as:

$$\begin{aligned} u_n(r)&=\frac{1}{2\pi}\int_{-\pi}^{\pi}u(r,\theta)e^{-in\theta}d\theta,\\ v_n(r)&=\frac{1}{2\pi}\int_{-\pi}^{\pi}v(r,\theta)e^{-in\theta}d\theta. \end{aligned} \tag{12}$$

and electric potential just depend on radius of composite rotating shaft. Therefore, Eq. (10c) confirms only for $n=0$ and will be omitted from the system of relations (10) for $n\neq 0$ [8].

For $n\neq 0$, substituting Eq. (11) into Eq. (10) gives:

$$d_1 u_n''+\frac{d_2}{r}u_n'+(\frac{d_3}{r^2}-n^2\frac{d_4}{r^2})u_n+in\frac{d_5}{r}v_n'+in\frac{d_6}{r^2}v_n=-\rho r\omega^2, \tag{13a}$$

$$d_9 v_n''+\frac{d_{10}}{r}v_n'+(\frac{d_{11}}{r^2}-n^2\frac{d_{12}}{r^2})v_n+in\frac{d_{13}}{r}u_n'+in\frac{d_{14}}{r^2}u_n=0. \tag{13b}$$

The solution of the above equations is assumed as [9]:

$$u_n(r)=Ar^{\eta},\qquad v_n(r)=Br^{\eta}. \tag{14}$$

where A and B are constants and obtain from boundary conditions. Substituting Eq. (14) into Eqs. (13), yields:

$$\left[d_1\,\eta(\eta-1)+d_2\eta+d_3-n^2 d_4 \right]A+\left[ind_5\eta+ind_6 \right]B=0,$$
$$\left[d_9\,\eta(\eta-1)+d_{10}\eta+d_{11}-n^2 d_{12} \right]B+\left[ind_{13}\eta+ind_{14} \right]A=0. \tag{15}$$

To obtain the nontrivial solution of Eqs. (15), the determinant of system should be equal to zero [9]. So four roots, η_{n1} to η_{n4} , are achieved and the general solutions are:

$$u_n(r)=\sum_{j=1}^{4} A_{nj} r^{\eta_{nj}}, \qquad v_n(r)=\sum_{j=1}^{4} M_{nj} A_{nj} r^{\eta_{nj}}. \tag{16}$$

where:

$$M_{nj}=-\frac{d_1\,\eta(\eta-1)+d_2\eta+d_3-n^2 d_4}{ind_5\eta+ind_6}, \tag{17}$$

For $n=0$, the equilibrium Eqs. (10) are reduced to:

$$d_1 u_0''+\frac{d_2}{r}u_0'+\frac{d_3}{r^2}u_0+d_7\,\phi_0''+\frac{d_8}{r}\phi_0''=-\rho r\omega^2, \tag{18a}$$
$$d_9 v_0''+\frac{d_{10}}{r}v_0'+\frac{d_{11}}{r^2}v_0=0, \tag{18b}$$
$$d_{16}\,\phi_0''+\frac{d_{17}}{r}\phi_0'+d_{18}\,u_0''+\frac{d_{19}}{r}u_0'=0. \tag{18c}$$

where the subscript zero indicates the solution for $n=0$. Two Eqs. (18a) and (18c) are a system of ordinary differential equations and the solution of this system is considered as [9]:

$$u_0(r)=A_0 r^{\eta_0}, \qquad \phi_0(r)=C_0 r^{\eta_0}. \tag{19}$$

Substituting Eq. (19) into Eqs. (18a) and (18c) yields:

$$\begin{aligned}&(d_1\eta_0(\eta_0-1)+d_2\eta_0+d_3)A_0+(d_7\eta_0(\eta_0-1)+d_8\eta_0)C_0=0,\\&(d_{16}\eta_0(\eta_0-1)+d_{17}\eta_0)C_0+(d_{18}\eta_0(\eta_0-1)+d_{19}\eta_0)A_0=0.\end{aligned} \tag{20}$$

To obtain the nontrivial solution of Eq. (20), the determinant of system should be equal to zero. So the four roots, η_{01} to η_{04} , are achieved and the general solutions are:

$$u_0(r)=\sum_{j=1}^{4} A_{0j} r^{\eta_{0j}},\ \phi_0(r)=\sum_{j=1}^{4} N_{0j} A_{0j} r^{\eta_{0j}}. \tag{21}$$

where

$$N_{0j}=-\frac{d_1\eta_0(\eta_0-1)+d_2\eta_0+d_3}{d_7\eta_0(\eta_0-1)+d_8\eta_0}. \tag{22}$$

For $n=0$ Eq. (18b) is a decoupled ordinary differential equation and the solution of this equation is considered as:

$$v_0(r)=\sum_{j=5}^{6} A_{0j} r^{\eta_{0j}}. \tag{23}$$

where

$$\eta_{05,06}=\frac{-d_{10}\pm\sqrt{{d_{10}}^2-4d_9d_{11}}}{2d_9}. \tag{24}$$

Finally substituting Eqs. (16) into Eq. (11) and using Eqs. (21) and (23), the general solutions for $u^g(r,\theta)$, $v^g(r,\theta)$ and $\phi^g(r)$ are expressed as:

$$u^g(r,\theta)=\sum_{j=1}^{4} A_{0j} r^{\eta_{0j}}+\sum_{n=-\infty,n\neq 0}^{\infty}\left[\sum_{j=1}^{4} A_{nj} r^{\eta_{nj}}\right]e^{in\theta}, \tag{25a}$$

$$v^g(r,\theta)=\sum_{j=5}^{6} A_{0j} r^{\eta_{0j}}+\sum_{n=-\infty,n\neq 0}^{\infty}\left[\sum_{j=1}^{4} M_{nj}\, A_{nj} r^{\eta_{nj}}\right]e^{in\theta}, \tag{25b}$$

$$\phi^g(r)=\sum_{j=1}^{4} N_{0j} A_{0j} r^{\eta_{0j}}. \tag{25c}$$

3.2 Particular solution

For $n\neq 0$, the particular solutions $u^p(r)$ and $v^p(r)$ are assumed as:

$${u_n}^p(r)=D_{n1}r^3, \qquad {v_n}^p(r)=D_{n2}r^3. \tag{26}$$

Substituting Eq. (26) into Eq. (13) and Equating the coefficients of the identical powers and using Cramer's method, D_{n1} and D_{n2} are obtained.

For $n=0$, the particular solutions $u^p(r)$, $v^p(r)$ and $\phi^p(r)$ are assumed as:

$${u_0}^p(r)=D_{01}r^3, \qquad {\phi_0}^p(r)=D_{03}r^3. \tag{27}$$

Substituting Eq. (27) into Eq. (18), D_{01} and D_{03} are determined.

The complete solutions for $u_n(r,\theta)$, $v_n(r,\theta)$ and $\phi(r)$ are the sum of the general and particular solutions as follows:

$$u_n(r,\theta)=\left[\sum_{j=1}^{4} A_{0j} r^{\eta_{0j}}+D_{01}r^3\right]+\sum_{n=-\infty,n\neq 0}^{\infty}\left[\sum_{j=1}^{4} A_{nj} r^{\eta_{nj}}+D_{n1}r^3\right]e^{in\theta}, \tag{28a}$$

$$v_n(r,\theta)=\left[\sum_{j=5}^{6} A_{0j} r^{\eta_{0j}}\right]+\sum_{n=-\infty,n\neq 0}^{\infty}\left[\sum_{j=1}^{4} M_{nj}\, A_{nj} r^{\eta_{nj}}+D_{n2}r^3\right]e^{in\theta}, \tag{28b}$$

$$\phi(r)=\sum_{j=1}^{4} N_{0j} A_{0j} r^{\eta_{0j}}+D_{03}r^3. \tag{28c}$$

Substituting Eqs. (28-a)- (28-c) into Eq. (1), the strains are obtained as:

$$\varepsilon_{rr} = \left[\sum_{j=1}^{4} \eta_{0j} A_{0j} r^{(\eta_{0j}-1)} + 3D_{01} r^2\right] + \sum_{n=-\infty, n\neq 0}^{\infty} \left[\sum_{j=1}^{4} \eta_{nj} A_{nj} r^{(\eta_{nj}-1)} + 3D_{n1} r^2\right] e^{in\theta}, \tag{29a}$$

$$\varepsilon_{\theta\theta} = \left[\sum_{j=1}^{4} A_{0j} r^{(\eta_{0j}-1)} + D_{01} r^2\right] + \sum_{n=-\infty, n\neq 0}^{\infty} \left[\sum_{j=1}^{4} A_{nj} r^{(\eta_{nj}-1)} + D_{n1} r^2\right] e^{in\theta} + in \sum_{n=-\infty, n\neq 0}^{\infty} \left[\sum_{j=1}^{4} M_{nj} A_{nj} r^{(\eta_{nj}-1)} + D_{n2} r^2\right] e^{in\theta}, \tag{29b}$$

$$\begin{aligned}\varepsilon_{r\theta} = {} & \frac{1}{2}\left\{ in \sum_{n=-\infty, n\neq 0}^{\infty} \left[\sum_{j=1}^{4} A_{nj} r^{(\eta_{nj}-1)} + D_{n1} r^2\right] e^{in\theta} + \sum_{j=5}^{6} \eta_{0j} A_{0j} r^{(\eta_{0j}-1)} \right\} \\ & + \frac{1}{2}\left\{ \sum_{n=-\infty, n\neq 0}^{\infty} \left[\sum_{j=1}^{4} \eta_{nj} M_{nj} A_{nj} r^{(\eta_{nj}-1)} + 3D_{n2} r^2\right] e^{in\theta} - \left[\sum_{j=5}^{6} A_{0j} r^{(\eta_{0j}-1)}\right] \right. \\ & \left. - \sum_{n=-\infty, n\neq 0}^{\infty} \left[\sum_{j=1}^{4} M_{nj} A_{nj} r^{(\eta_{nj}-1)} + D_{n2} r^2\right] e^{in\theta} \right\}.\end{aligned} \tag{29c}$$

Substituting Eq. (28c) into Eq. (6) and using Eqs. (29a)-(29c), the stress components and the electrical displacement in radial direction are calculated that presented in Appendix B.

It is recalled that stress components contain six unknown constants A_{nj} $(j = 1,...,6)$ and therefore to evaluate these constants, six boundary conditions that may be either the given displacements or stresses, or combinations are required. Expanding the given boundary conditions in complex Fourier series gives [9]:

$$g_j(\theta) = \sum_{n=-\infty}^{\infty} G_j(n) e^{in\theta}, \quad j = 1,...,6, \tag{30}$$

where

$$G_j(n) = \frac{1}{2\pi} \int_{-\pi}^{\pi} g_j(\theta) e^{-in\theta} d\theta, \quad j = 1,...,6. \tag{31}$$

Constants A_{nj} are calculated using Eqs. (30) and (31).

4 NUMERICAL RESULTS

Consider a thick-walled rotating shaft with inner and outer radius $a = 1m$ and $b = 1.2m$, respectively [9]. In this study, the PZT-4 has been considered as smart matrix and BNNT has been taken into account for fiber of the composite. In order to examine the selected matrix, the stress analysis for composite rotating shaft made of PVDF is performed and the results are compared with PZT-4. Mechanical and electrical properties of PZT-4, BNNT and PVDF are listed in Table 1 [3, 5, 13].

In order to examine the proposed solution, it is considered the effect of two-dimensional mechanical behavior of piezoelectric composite rotating shaft. The inside and outside boundary conditions are expressed as [8]:

Table 1
Material and electrical properties for PZT-4, PVDF and BNNT

	PZT-4 [3]	PVDF [5, 14]	BNNT [5]
$C_{11}(GPa)$	139	238.24	2035
$C_{13}(GPa)$	74.3	2.19	692
$C_{33}(GPa)$	115	10.64	2035
$e_{31}(C/m^2)$	-5.2	-0.13	0
$e_{33}(C/m^2)$	15.1	-0.276	0.95
$\in_{33}/\in_0$	634.728	11.98	1250
$\rho(g/cm^3)$	7.5	1.78	1.37

$\in_0 = 8.854185 \times 10^{-12}(F/m)$

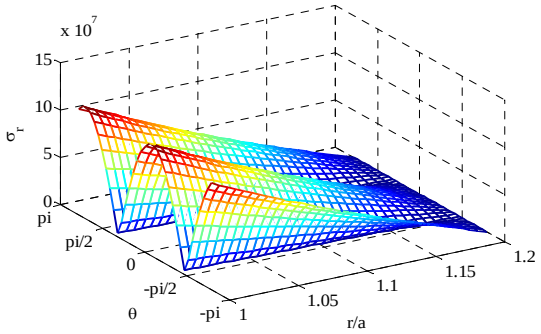

Fig. 2
Distribution of radial stress in composite rotating shaft subjected to non-axisymmetric internal pressure.

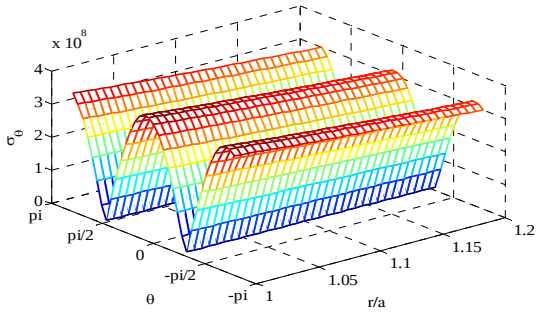

Fig. 3
Distribution of circumferential stress in composite rotating shaft subjected to non-axisymmetric internal pressure.

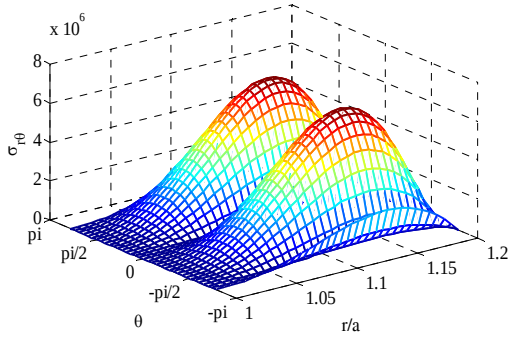

Fig. 4
Distribution of shear stress in composite rotating shaft subjected to non-axisymmetric internal pressure.

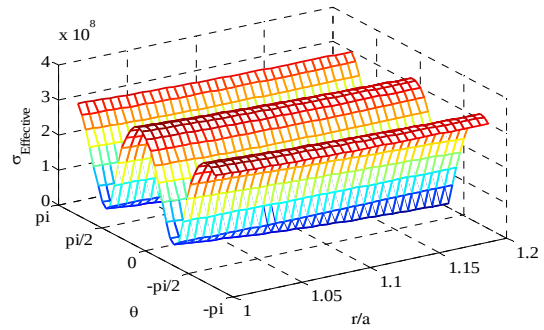

Fig. 5
Distribution of effective stress in composite rotating shaft subjected to non-axisymmetric internal pressure.

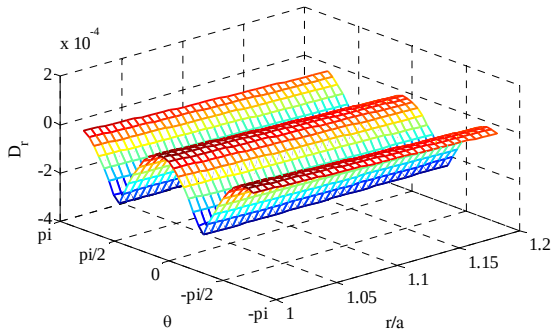

Fig. 6
Distribution of radial electric displacement in composite rotating shaft subjected to non-axisymmetric internal pressure.

$$\begin{aligned} &S_{rr}(r=a)=100\cos^2\theta\ \ Mpa,\ \ S_{rr}(r=b)=0,\\ &S_{r\theta}(r=a)=0,\quad S_{r\theta}(r=b)=0,\\ &\phi(r=a)=1000v,\ \phi(r=b)=0. \end{aligned} \tag{32}$$

Figs. 2-4 demonstrate the distribution of radial, circumferential and shear stresses. It is evident that all components of stresses follow from a harmonic pattern. Also, it is found from these figures that the boundary conditions in inner and outer surfaces of composite rotating shaft have been satisfied. Effective stress that is calculated by Von-Mises yield criterion has been illustrated in Fig. 5. As expected, effective stress follows from a harmonic pattern.

Fig. 6 shows electric displacement distribution along the radius and circumferential directions. It is also noted that the patterns of Figs.2-6 are consistent with reference [9].According to general boundary conditions Eq. (32), the inside and outside boundary conditions have been simplified to study the effect of angular velocity, volume fraction and orientation angle of BNNTs and electric potential on Von-Mises stress in composite rotating shaft, as follows:

$$\begin{aligned} &S_{rr}(r=a)=100Mpa,\ S_{rr}(r=b)=0,\\ &S_{r\theta}(r=a)=0,\ \ S_{r\theta}(r=b)=0,\\ &\phi(r=a)=100v,\ \phi(r=b)=0. \end{aligned} \tag{33}$$

Figs. 7 and 8 depict the effect of angular velocity on radial and circumferential stress distribution in composite rotating shaft made of PZT-4 and PVDF for three different values of ω . It can be seen from these figures that the magnitude of stresses for composite shaft made of PVDF is more remarkable than PZT-4. Nevertheless, the behavior of stresses for two kind of composite matrix is similar.

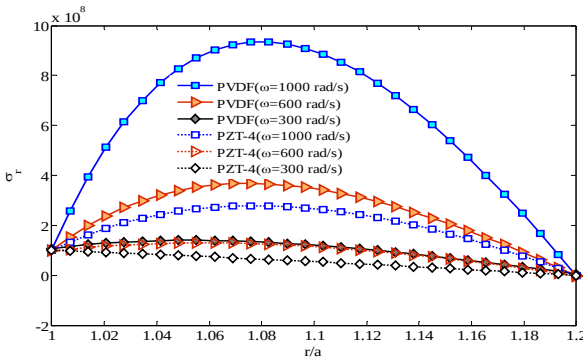

Fig. 7
Comparison of radial stress distribution in composite rotating shaft made of PZT-4 and PVDF for three different values of ω .

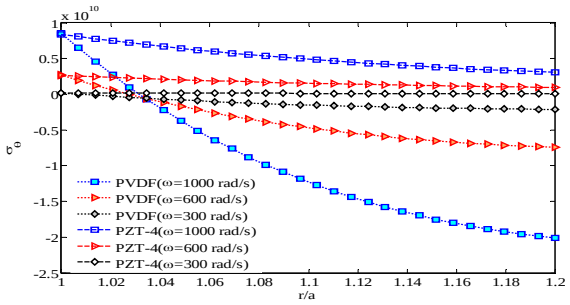

Fig. 8
Comparison of circumferential stress distribution in composite rotating shaft made of PZT-4 and PVDF for three different values of ω .

Table 2
Maximum effective stress for composite rotating shaft made of PZT_4 and PVDF

Angular velocity	Maximum Effective Stress			
	PZT-4		PVDF	
	Magnitude	*Position*	*Magnitude*	*Position*
$\omega = 0$	1.7510×10^{8}	*inner radius*	3.1396×10^{8}	*outer radius*
$\omega = 300\frac{rad}{s}$	6.6455×10^{8}	*inner radius*	2.0982×10^{9}	*outer radius*
$\omega = 600\frac{rad}{s}$	2.5868×10^{9}	*inner radius*	7.4509×10^{9}	*outer radius*
$\omega = 1000\frac{rad}{s}$	8.3534×10^{9}	*inner radius*	2.0139×10^{10}	*outer radius*

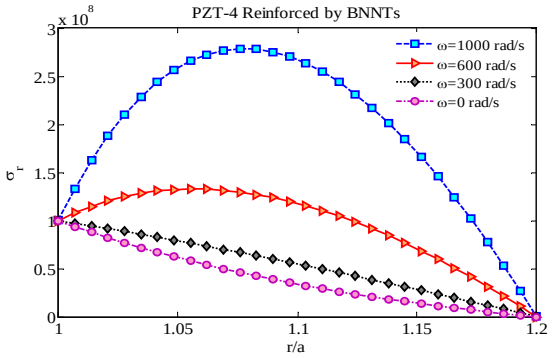

Fig. 9
The effect of angular velocity on radial stress in composite rotating shaft made of PZT-4 reinforced by BNNTs.

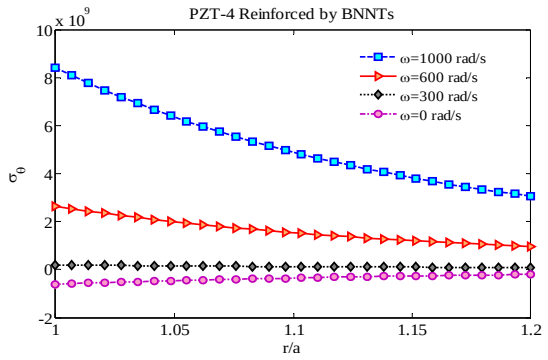

Fig. 10
The effect of angular velocity on circumferential stress in composite rotating shaft made of PZT-4 reinforced by BNNTs.

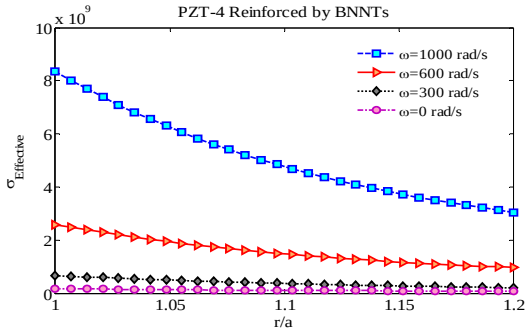

Fig. 11
The effect of angular velocity on effective stress in composite rotating shaft made of PZT-4 reinforced by BNNTs.

Table 2 shows the maximum effective stress at inner and outer radius of composite rotating shaft made of PZT-4 and PVDF. By comparison with the results it can be found that maximum effective stress for composite shaft made of PVDF occurs in outer radii while for composite shaft with PZT-4 matrix takes place on inner radius of rotating shaft. Figs. 9-11 illustrate the effect of angular velocity on radial, circumferential and effective stresses in composite rotating shaft. It can be seen from these figures that increasing angular velocity leads to increase all components of stresses and decrease stability of this structure.

Fig. 12 shows the effect of volume fraction on Von-Mises stress in composite rotating shaft. It can be seen from this figure that increasing volume content of BNNTs causes to decrease Von-Mises stress and has a significant effect on strength of composite structure. Designers could meet their purposes by selecting the suitable percent of fiber in composite cylinder. Fig. 13 illustrates the effect of orientation angle of BNNTs on effective stress in composite rotating shaft. The orientation angle of fiber in composite is very important because it can be affected on mechanical behavior of composite. This composite structure has been reinforced by BNNTs that can be aligned in different direction. Since the purpose is stress analyzing, the angle is the best at which stress is reduced. In addition, it can be concluded from this figure that due to the significant radial piezoelectricity effect of BNNT, the effective stress of the composite is declined by increasing angle of BNNTs with respect to longitudinal axis of rotating shaft.

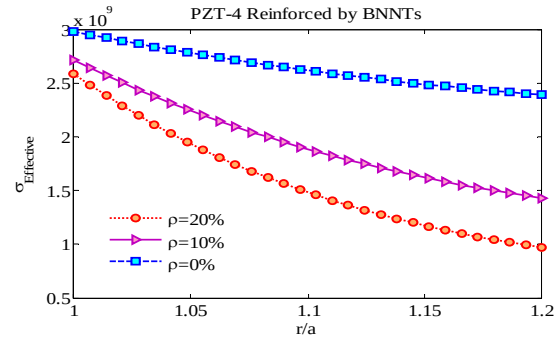

Fig. 12
The effect of volume fraction of BNNTs on the effective stress in composite rotating shaft.

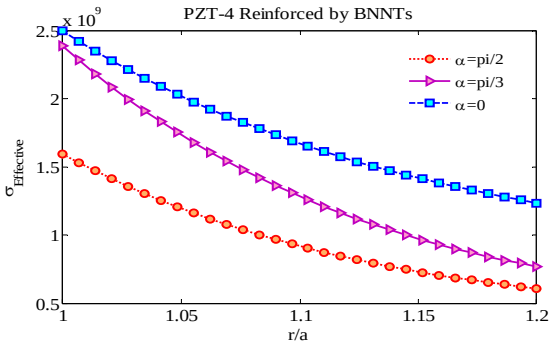

Fig. 13
The effect of orientation angle of BNNTs on the effective stress in composite rotating shaft.

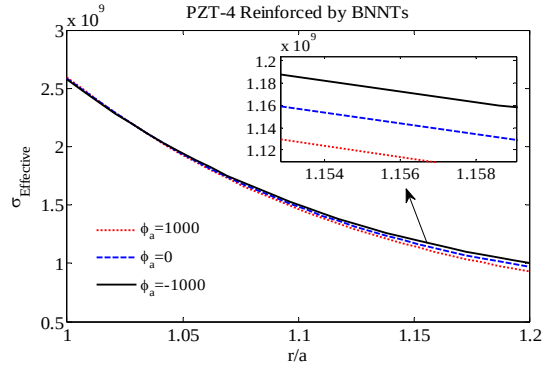

Fig. 14
The effect of electric potential on the effective stress in composite rotating shaft.

The effect of electric potential on the Von-Mises stress in composite rotating shaft is investigated in Fig. 14. where the presence of positive electric potential has been considered as a factor for decreasing effective stress and increasing resistance of composite structure.

5 CONCLUSION

General theoretical analysis of two-dimensional non-axisymmetric mechanical stresses for a thick-walled composite rotating shaft reinforced by BNNT is developed, where BNNTs are arranged in a radial direction inside of PZT-4 matrix. Higher order governing equations were solved analytically by Fourier series and the results illustrate distribution of mechanical stresses. Regarding reinforcement of composite, it can be observed that using BNNTs as a fiber and its orientation angle with respect to composite shaft axis have significant effects on the mechanical behavior of the system. The results indicated that the effective stress is strongly dependent on the angular velocity so that decreasing the magnitude of angular velocity significantly decreases the Von-Mises stress. Also it is concluded that imposing positive electric potential caused to decrease effective stress and increase stability of system. Therefore applying the positive electric potential can be used as well as controlling parameters to improve the fatigue life of the composite rotating shaft. In addition, the results of this study show considering the special boundary conditions for a composite rotating shaft, the mechanical stresses and electrical displacement can be controlled and optimized to design and use this kind of structures.

APPENDIX A

$$[Q]=[T]\left[\tilde{Q}\right][T]^{T}=\begin{bmatrix} Q_{11} & Q_{12} & Q_{13} & Q_{14} \\ Q_{21} & Q_{22} & Q_{23} & Q_{24} \\ Q_{31} & Q_{32} & Q_{33} & Q_{34} \\ Q_{41} & Q_{42} & Q_{43} & Q_{44} \end{bmatrix}.$$

$$\begin{aligned} &d_1 = Q_{11}, && d_2 = Q_{12}+Q_{11}-Q_{21}, && d_3 = -d_{12} = -Q_{22}, && d_4 = Q_{33}, \\ &d_5 = Q_{12}+Q_{33}, && d_6 = -(Q_{33}+Q_{22}), && d_7 = -Q_{14}, && d_8 = -(Q_{14}-Q_{24}), \\ &d_9 = d_{10} = -d_{11} = Q_{33}, && d_{13} = Q_{21}+Q_{33}, && d_{14} = Q_{22}+Q_{33}, && d_{15} = -Q_{24}, \\ &d_{16} = d_{17} = -Q_{44}. && d_{18} = Q_{41}, && d_{19} = Q_{41}+Q_{42}, && d_{20} = Q_{42}. \end{aligned} \tag{A.1}$$

APPENDIX B

$$\begin{aligned} \sigma_{rr} = {} & Q_{11}\left\{\sum_{j=1}^{4}\eta_{0j}A_{0j}r^{(\eta_{0j}-1)}+3D_{01}r^2+\sum_{n=-\infty,n\neq 0}^{\infty}\left[\sum_{j=1}^{4}\eta_{nj}A_{nj}r^{(\eta_{nj}-1)}+3D_{n1}r^2\right]e^{in\theta}\right\}+ \\ & Q_{12}\left\{\begin{matrix}\sum_{j=1}^{4}A_{0j}r^{(\eta_{0j}-1)}+D_{01}r^2+ \\ \sum_{n=-\infty,n\neq 0}^{\infty}\left[\sum_{j=1}^{4}A_{nj}r^{(\eta_{nj}-1)}+D_{n1}r^2\right]e^{in\theta}\end{matrix}+in\sum_{n=-\infty,n\neq 0}^{\infty}\left[\sum_{j=1}^{4}M_{nj}A_{nj}r^{(\eta_{nj}-1)}+D_{n2}r^2\right]e^{in\theta}\right\}+ \\ & Q_{13}\left\{\frac{1}{2}\left\{in\sum_{n=-\infty,n\neq 0}^{\infty}\left[\sum_{j=1}^{4}A_{nj}r^{(\eta_{nj}-1)}+D_{n1}r^2\right]e^{in\theta}+\sum_{j=5}^{6}\eta_{0j}A_{0j}r^{(\eta_{0j}-1)}\right\}+\frac{1}{2}\left\{\sum_{n=-\infty,n\neq 0}^{\infty}\left[\sum_{j=1}^{4}\eta_{nj}M_{nj}A_{nj}r^{(\eta_{nj}-1)}+3D_{n2}r^2\right]e^{in\theta}-\right.\right. \\ & \left.\left.\left[\sum_{j=5}^{6}A_{0j}r^{(\eta_{0j}-1)}\right]-\sum_{n=-\infty,n\neq 0}^{\infty}\left[\sum_{j=1}^{4}M_{nj}A_{nj}r^{(\eta_{nj}-1)}+D_{n2}r^2\right]e^{in\theta}\right\}-Q_{14}\left\{\sum_{j=1}^{4}N_{0j}\eta_{0j}A_{0j}r^{\eta_{0j}-1}+3D_{03}r^2\right\}, \end{aligned}$$

$$\begin{aligned} \sigma_{\theta\theta} = {} & Q_{21}\left\{\sum_{j=1}^{4}\eta_{0j}A_{0j}r^{(\eta_{0j}-1)}+3D_{01}r^2+\sum_{n=-\infty,n\neq 0}^{\infty}\left[\sum_{j=1}^{4}\eta_{nj}A_{nj}r^{(\eta_{nj}-1)}+3D_{n1}r^2\right]e^{in\theta}\right\}+ \\ & Q_{22}\left\{\begin{matrix}\sum_{j=1}^{4}A_{0j}r^{(\eta_{0j}-1)}+D_{01}r^2+ \\ \sum_{n=-\infty,n\neq 0}^{\infty}\left[\sum_{j=1}^{4}A_{nj}r^{(\eta_{nj}-1)}+D_{n1}r^2\right]e^{in\theta}\end{matrix}+in\sum_{n=-\infty,n\neq 0}^{\infty}\left[\sum_{j=1}^{4}M_{nj}A_{nj}r^{(\eta_{nj}-1)}+D_{n2}r^2\right]e^{in\theta}\right\}+ \\ & Q_{23}\left\{\frac{1}{2}\left\{in\sum_{n=-\infty,n\neq 0}^{\infty}\left[\sum_{j=1}^{4}A_{nj}r^{(\eta_{nj}-1)}+D_{n1}r^2\right]e^{in\theta}+\sum_{j=5}^{6}\eta_{0j}A_{0j}r^{(\eta_{0j}-1)}\right\}+\frac{1}{2}\left\{\sum_{n=-\infty,n\neq 0}^{\infty}\left[\sum_{j=1}^{4}\eta_{nj}M_{nj}A_{nj}r^{(\eta_{nj}-1)}+3D_{n2}r^2\right]e^{in\theta}-\right.\right. \\ & \left.\left.\left[\sum_{j=5}^{6}A_{0j}r^{(\eta_{0j}-1)}\right]-\sum_{n=-\infty,n\neq 0}^{\infty}\left[\sum_{j=1}^{4}M_{nj}A_{nj}r^{(\eta_{nj}-1)}+D_{n2}r^2\right]e^{in\theta}\right\}-Q_{24}\left\{\sum_{j=1}^{4}N_{0j}\eta_{0j}A_{0j}r^{\eta_{0j}-1}+3D_{03}r^2\right\}, \end{aligned}$$

$$\sigma_{r\theta} = Q_{31}\left\{\sum_{j=1}^{4}\eta_{0j}A_{0j}r^{(\eta_{0j}-1)} + 3D_{01}r^2 + \sum_{n=-\infty,n\neq 0}^{\infty}\left[\sum_{j=1}^{4}\eta_{nj}A_{nj}r^{(\eta_{nj}-1)} + 3D_{n1}r^2\right]e^{in\theta}\right\} +$$

$$Q_{32}\left\{\begin{array}{l}\sum_{j=1}^{4}A_{0j}r^{(\eta_{0j}-1)} + D_{01}r^2 + \\ \sum_{n=-\infty,n\neq 0}^{\infty}\left[\sum_{j=1}^{4}A_{nj}r^{(\eta_{nj}-1)} + D_{n1}r^2\right]e^{in\theta}\end{array} + in\sum_{n=-\infty,n\neq 0}^{\infty}\left[\sum_{j=1}^{4}M_{nj}\,A_{nj}r^{(\eta_{nj}-1)} + D_{n2}r^2\right]e^{in\theta}\right\} +$$

$$Q_{33}\left\{\frac{1}{2}\left\{in\sum_{n=-\infty,n\neq 0}^{\infty}\left[\sum_{j=1}^{4}A_{nj}r^{(\eta_{nj}-1)} + D_{n1}r^2\right]e^{in\theta} + \sum_{j=5}^{6}\eta_{0j}A_{0j}r^{(\eta_{0j}-1)}\right\} + \frac{1}{2}\left\{\sum_{n=-\infty,n\neq 0}^{\infty}\left[\sum_{j=1}^{4}\eta_{nj}M_{nj}\,A_{nj}r^{(\eta_{nj}-1)} + 3D_{n2}r^2\right]e^{in\theta} - \right.\right.$$

$$\left.\left.\left[\sum_{j=5}^{6}A_{0j}r^{(\eta_{0j}-1)}\right] - \sum_{n=-\infty,n\neq 0}^{\infty}\left[\sum_{j=1}^{4}M_{nj}\,A_{nj}r^{(\eta_{nj}-1)} + D_{n2}r^2\right]e^{in\theta}\right\} - Q_{34}\left\{\sum_{j=1}^{4}N_{0j}\,\eta_{0j}A_{0j}r^{\eta_{0j}-1} + 3D_{03}\,r^2\right\},$$

$$D_r = Q_{41}\left\{\sum_{j=1}^{4}\eta_{0j}A_{0j}r^{(\eta_{0j}-1)} + 3D_{01}r^2 + \sum_{n=-\infty,n\neq 0}^{\infty}\left[\sum_{j=1}^{4}\eta_{nj}A_{nj}r^{(\eta_{nj}-1)} + 3D_{n1}r^2\right]e^{in\theta}\right\} +$$

$$Q_{42}\left\{\begin{array}{l}\sum_{j=1}^{4}A_{0j}r^{(\eta_{0j}-1)} + D_{01}r^2 + \\ \sum_{n=-\infty,n\neq 0}^{\infty}\left[\sum_{j=1}^{4}A_{nj}r^{(\eta_{nj}-1)} + D_{n1}r^2\right]e^{in\theta}\end{array} + in\sum_{n=-\infty,n\neq 0}^{\infty}\left[\sum_{j=1}^{4}M_{nj}\,A_{nj}r^{(\eta_{nj}-1)} + D_{n2}r^2\right]e^{in\theta}\right\} +$$

$$Q_{43}\left\{\frac{1}{2}\left\{in\sum_{n=-\infty,n\neq 0}^{\infty}\left[\sum_{j=1}^{4}A_{nj}r^{(\eta_{nj}-1)} + D_{n1}r^2\right]e^{in\theta} + \sum_{j=5}^{6}\eta_{0j}A_{0j}r^{(\eta_{0j}-1)}\right\} + \frac{1}{2}\left\{\sum_{n=-\infty,n\neq 0}^{\infty}\left[\sum_{j=1}^{4}\eta_{nj}M_{nj}\,A_{nj}r^{(\eta_{nj}-1)} + 3D_{n2}r^2\right]e^{in\theta} - \right.\right.$$

$$\left.\left.\left[\sum_{j=5}^{6}A_{0j}r^{(\eta_{0j}-1)}\right] - \sum_{n=-\infty,n\neq 0}^{\infty}\left[\sum_{j=1}^{4}M_{nj}\,A_{nj}r^{(\eta_{nj}-1)} + D_{n2}r^2\right]e^{in\theta}\right\} - Q_{44}\left\{\sum_{j=1}^{4}N_{0j}\,\eta_{0j}A_{0j}r^{\eta_{0j}-1} + 3D_{03}\,r^2\right\}.$$

(B.1)

ACKNOWLEDGEMENTS

The authors are grateful to University of Kashan for supporting this work by Grant No. 65475/53. They would also like to thank the Iranian Nanotechnology Development Committee for their financial support. This research was supported by the Thermoelasticity Center of Excellence, Mechanical Engineering Department, Amirkabir University of Technology.

REFERENCES

[1] Bayat M., Saleem M., Sahari B.B., Hamouda A.M.S., Mahdi E., 2009, Mechanical and thermal stresses in a functionally graded rotating disk with variable thickness due to radially symmetry loads, *International Journal of Pressure Vessels and Piping* **86**: 357-372.

[2] Hojjati M.H., Jafari S., 2009, Semi-exact solution of non-uniform thickness and density rotating disks, Part II: Elastic strain hardening solution, *International Journal of Pressure Vessels and Piping* **86**: 307-318.

[3] Babaei M.H., Chen Z.T., 2008, Analytical solution for the electromechanical behavior of a rotating functionally graded piezoelectric hollow shaft, *Archive of Applied Mechanics* **78**: 489-500.

[4] Ghorbanpour Arani A., Kolahchi R., Mosallaie Barzoki A.A., 2011, Effect of material in-homogeneity on electro-thermo-mechanical behaviors of functionally graded piezoelectric rotating shaft, *Applied Mathematical Modelling* **35**: 2771–2789.

[5] Ghorbanpour Arani A., Shajari A.R., Amir S., Loghman A., 2013, Electro-thermo-mechanical nonlinear nonlocal vibration and instability of embedded micro-tube reinforced by BNNT conveying fluid, *Physica E* **44**: 424-432.

[6] Akis T., Eraslan A.N., 2006, The stress response and onset of yield of rotating FGM hollow shafts, *Acta Mechanica* **187**: 169-187.

[7] Ghorbanpour Arani A., Bakhtiari R., Mohammadimehr M., Mozdianfard M.R., 2011, Electro-magneto-mechanical responses of a radially polarized rotating functionally graded piezoelectric shaft, *Turkish Journal of Engineering and Environmental Sciences* **35**: 1-12.

[8] Atrian A., Jafari Fesharaki J., Majzoobi G.H., Sheidaee M., 2011, Effects of electric potential on thermo-mechanical behavior of functionally graded piezoelectric hollow cylinder under non-axisymmetric loads, *World Academy of Science, Engineering and Technology* **59**: 964-967.

[9] Jafari Fesharaki J., Jafari Fesharaki V., Yazdipoor M., Razavian B., 2012, Two-dimensional solution for electro-mechanical behavior of functionally graded piezoelectric hollow cylinder, *Applied Mathematical Modelling* **36**: 5521-5533.

[10] Tan P., Tong L., 2001, Micro-electro-mechanics models for piezoelectric-fiber-reinforced composite materials, *Composite Science Technology* **61**: 759-69.

[11] Tan P., Tong L., 2001, Micromechanics models for nonlinear behavior of piezoelectric fiber reinforced composite materials, *International Journal of Solids and Structures* **38**: 8999-9032.

[12] Ghorbanpour Arani A., Shajari A.R., Atabakhshian V., Amir S., Loghman A., 2013, Nonlinear dynamical response of embedded fluid -conveyed micro-tube reinforced by BNNTs, *Composites: Part B* **44**: 424-432.